buildings

MDPI

Article

Local Stability Analysis of a Composite Corrugated Steel Plate Pipe-Arch in Soil

Chengwen Che [1], Pingping Hu [1], Feng Shi [2], Pengsen Xu [2], Junxiu Liu [2] and Kai Li [2,*]

[1] China First Highway Engineering Co., Ltd., Beijing 100024, China; 13256961846@ccccltd.cn (C.C.); 18507060206@ccccltd.cn (P.H.)
[2] College of Civil Engineering, Anhui Jianzhu University, Hefei 230601, China; sf@stu.ahjzu.edu.cn (F.S.); xps@stu.ahjzu.edu.cn (P.X.); tjuliu@ahjzu.edu.cn (J.L.)
* Correspondence: kli@ahjzu.edu.cn

Abstract: The straight part of the corrugated steel plate (CSP) pipe-arch structure in soil may cause local buckling instability due to insufficient load-bearing capacity. Recently, composite CSP pipe-arch has been widely utilized to enhance structural stability, and their stability needs to be thoroughly investigated. This paper studies the local buckling stability problem of the straight part of composite CSP pipe-arch in soil by simplifying the soil support and introducing the inter-layer bonding effect. Based on elastic stability theory, a theoretical mechanical model of composite CSP pipe-arch was proposed. The Rayleigh–Ritz method and the semi-combined composite structure stiffness approximation were used to derive the critical buckling conditions for the straight part of the composite CSP pipe-arch. Through numerical calculation and influencing factors analysis, it is concluded that the critical buckling load of the straight part of the composite CSP pipe-arch structure is affected by the elastic modulus, thickness, Poisson's ratio, rotational restraint stiffness and side length of the straight part of the material. In particular, it is found that as the inter-layer bonding coefficient increases, the critical buckling load is improved, while the critical buckling wave number is mainly influenced by the width of the straight part, elastic modulus, and inter-layer bonding coefficient. Additionally, we discussed the coupling effect of several key parameters on the stability of the structure. The results of this study offer theoretical foundations and guidance for the application of composite CSP pipe-arch in soil engineering, such as culverts, tunnels, and pipeline transportation.

Keywords: corrugated steel plate pipe-arch; composite structure; inter-layer bonding; local buckling stability; critical buckling load

check for updates

Citation: Che, C.; Hu, P.; Shi, F.; Xu, P.; Liu, J.; Li, K. Local Stability Analysis of a Composite Corrugated Steel Plate Pipe-Arch in Soil. *Buildings* **2024**, *14*, 3290. https://doi.org/10.3390/buildings14103290

Academic Editor: Hiroshi Tagawa

Received: 1 August 2024
Revised: 4 September 2024
Accepted: 16 October 2024
Published: 17 October 2024

Copyright: © 2024 by the authors. Licensee MDPI, Basel, Switzerland. This article is an open access article distributed under the terms and conditions of the Creative Commons Attribution (CC BY) license (https://creativecommons.org/licenses/by/4.0/).

1. Introduction

Most highway passages, pipe culverts, tunnels, and bridge projects are made of reinforced concrete materials. However, there are common shortcomings, such as high structural cost, long construction and maintenance periods, many prefabricated structural joints, and difficulty in joint sealing [1,2]. These issues can lead to cracking, water leakage, and high maintenance costs during use [3,4]. As a unique and versatile building material, corrugated steel plate (CSP) has the advantages of being lightweight [5], high strength [6,7], low cost [8], corrosion resistance [9,10] and strong adaptability [11–13]. CSP can greatly improve structural strength, stiffness and stability in the design and construction of culverts [14,15], bridges [16,17] and shear walls [18,19] and has become a powerful substitute for traditional reinforced concrete materials [20–22]. However, with the increasing application of CSP structures in these fields, its stability problems have gradually emerged. Precise stability analysis of CSP pipe-arch has become particularly important [23–26]. This is not only related to the safety and reliability of the engineering structure but also directly affects the economic benefits and maintenance costs of the project.

Currently, many scholars have conducted extensive research on the buckling stability of CSP [27–30]. Machimdamrong et al. [31] proposed a formula for calculating the elastic

shear buckling capacity of corrugated plates with elastically rotationally restrained edges. Using the Rayleigh–Ritz method, they modeled the corrugated plate as an orthotropic Mindlin plate, with rotational springs simulating the elastic rotational restraints at the edges. The study results encompass the general case of elastic rotational restraints at the boundary edges and align with existing formulas for the limiting cases of simply supported and clamped edges. Dou et al. [32,33] used the finite element analysis method to study the shear buckling behavior of CSP shear walls and proposed a fitting equation to predict the elastic shear buckling capacity of sinusoidal CSP. It is found that the corrugation repetition number parameter, which has been ignored in previous studies, has a significant impact on the elastic shear buckling load. Chen et al. [15] investigated the local buckling stability of the straight parts of corrugated steel pipe-arches in soil. By establishing a local finite element model of the pipe-arch, the effects of plate thickness, corrugation, aspect ratio, and curvature on the local buckling load of corrugated steel were studied, revealing that the actual rotational restraint is negative. They also proposed reasonable limits for the width-to-thickness ratio of the straight parts of corrugated steel to prevent local buckling in these regions of the pipe-arches. Li et al. [34] studied the bearing capacity and failure mode of CSP through experimental testing and theoretical analysis. By considering the effects of concentrated load and bending stress on the bearing capacity of corrugated steel, they obtained the local buckling calculation formula. The local buckling calculation results are compared with the test results to verify the reliability of the local buckling calculation formula. Bi et al. [35] derived the elastic buckling stress calculation formula of a single CSP through theoretical analysis, gave the optimal parameter values for the local buckling stability of corrugated steel, and compared them with test results and finite element analysis to verify the rationality of the theoretical formula. Guo et al. [36] studied the local elastic shear buckling strength of trapezoidal corrugated steel webs through finite element and theoretical analysis. They found that the fold-width ratio (defined as the longitudinal fold-width divided by the inclined fold-width) significantly affects the local elastic shear buckling strength. When the fold-width ratio is greater than 1.0, the commonly used local elastic shear buckling coefficient greatly underestimates the local shear buckling strength. Based on the finite element analysis results, they proposed an improved formula for calculating the local shear buckling strength.

As engineering technology advances, composite CSP pipe-arches have become a common structural form to meet quality and efficiency demands. These arches are made from composite material plates, typically consisting of an upper steel layer and a lower layer of other materials, chosen based on specific application needs. For instance, steel and concrete are bonded using high-strength bolts [37], combining the strength and light weight of steel with concrete's corrosion resistance. Additionally, as shown in Figure 1, steel can be bonded with other metals through processes like rolling, welding, and adhesive bonding, significantly improving properties such as wear resistance and thermal expansion of the corrugated pipe. These structures combine the lightweight and durability of CSP pipe-arch with the mechanical properties of composite layer materials, thereby enhancing the load-bearing capacity and stability of the structure. This results in significant economic benefits in engineering construction [38–41]. Researchers have conducted a large number of experimental and theoretical studies on the composite structure of corrugated steel-composite layers and deeply explored the stability performance of different composite CSP pipe-arch [42–45]. As shown in Figure 2, El-Taher's [46] study examines the effects of corrosion and erosion on the stability of composite metal corrugated culverts, revealing that corrosion-induced local buckling may occur before global buckling. The study also provides a preliminary equation for assessing local buckling, helping engineers more accurately evaluate culvert stability. Wang et al. [47] investigated the compressive buckling behavior of CSP-concrete composite structures in contact with a rigid medium through finite element analysis and theoretical derivation. They validated the numerical results with experimental data and proposed design formulas for the strength reduction factor of CSPs and the upper limit of the normalized slenderness ratio for compact sections. These

findings provide a basis for the stability design of CSP-concrete composite structures under compressive and bending moments.

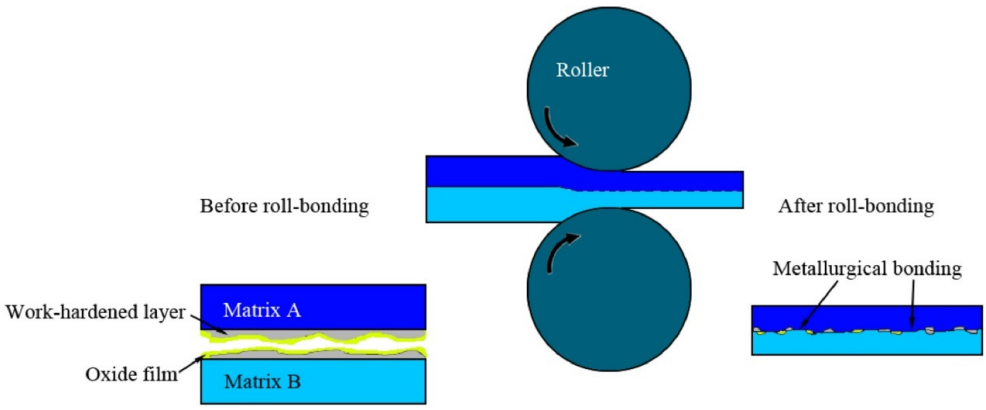


Figure 1. Schematic of Mg/Al laminated metal composites fabricated by roll-bonding [37].



Figure 2. Typical invert corrosion of corrugated metal culvert [46].

Furthermore, Kheirikhah et al. [48] studied the bending and buckling behavior of laminated composite plate corrugated soft-core sandwich plates under uniaxial loading. By using ANSYS 12.0. to conduct finite element analysis of the sandwich plate, the effects of corrugation shape, plate stack structure, boundary conditions, and plate length-to-thickness ratio on the bending behavior and linear uniaxial buckling load of the sandwich plate were numerically studied. The study found that CSP can significantly improve the linear uniaxial buckling capacity of sandwich plates and that trapezoidal corrugations are more prominent than sinusoidal corrugations. Guo et al. [49] filled concrete into the space between double CSPs to construct a new composite wall (CDSCW). By conducting finite element eigenvalue buckling analysis, the overall elastic buckling behavior of CDSCW under vertical compressive load was studied. According to Euler's formula, the estimation formula of the elastic buckling load of CDSCW and the corresponding normalized slenderness ratio λ_n were obtained. Through finite element nonlinear analysis, the overall unstable performance of CDSCW under compression conditions was studied, and the overall stability coefficient φ and the φ-λ_n curve used for strength design were obtained. Liu et al. [50] established a model of a CSP ordinary concrete slab and two different CSP-concrete composite structures. Through theoretical derivation and experimental analysis, they found that compared to ordinary concrete composite structures, CSP-rubber concrete composite structures have lower flexural and compressive stiffness, larger deflections, higher steel stresses, and lower

concrete stresses. Additionally, they exhibit better energy dissipation capabilities, making them suitable as seismic-resistant structural materials. Zhang et al. [51] studied the bending behavior and longitudinal shear mechanism of sinusoidal CSP composite plates. The study found that the flexural strength of CSP-concrete composite plates is positively related to the number of shear connectors and the thickness of the concrete cover, but continued increase in the thickness of the concrete cover may lead to longitudinal shear failure. Sun et al. [52] proposed a new type of corrugated steel-concrete (CSC) integrated pipe gallery. Through theoretical analysis of cross-sectional characteristics, it was found that the joint action of corrugated steel and concrete can greatly increase the structural stiffness, reaching 1.43 times that of simple superposition of corrugated steel and concrete, respectively. In summary, with the development of engineering technology, it is particularly important to study the mechanical properties and buckling stability of CSP-composite layer composite structures.

Although CSP pipe-arch structures have been extensively studied, most of the research has focused on single-layer CSP pipe-arch structures, with relatively few studies on composite CSP pipe-arch structures. Furthermore, for buried CSP pipe-arch structures in soil, the width-to-thickness ratio of the straight part of the section can be relatively large, leading to the possibility of local buckling in the straight part before the overall bearing capacity is reached, thereby reducing the structural bearing capacity [53]. Therefore, it is necessary to conduct an in-depth study on the local buckling behavior of the straight part of composite CSP pipe-arch structures in soil. This paper aims to analyze the local buckling behavior of the straight part of composite CSP pipe-arch structures subjected to external loads in soil, thereby providing theoretical support for practical engineering design.

This paper primarily considers the issue of local buckling in composite CSP pipe-arch structures under external loads, such as vehicle and soil loads, in underground engineering projects like tunnels and culverts. When the structure is subjected to these external loads, significant uniform forces may develop along the edges of the straight part of the composite CSP pipe-arch. This could lead to local instability before the structure reaches its ultimate load-bearing capacity, thereby reducing the overall structural capacity [53]. Therefore, it is necessary to theoretically solve for the magnitude of uniform forces along the edges of the straight part of the composite CSP pipe-arch. Based on the theory of elastic stability [54] and the theory of ring compression [55], a theoretical mechanical model of the composite CSP pipe-arch is constructed. Using the Rayleigh–Ritz method and an approximate calculation method for the stiffness of semi-combined composite structures, theoretical formulas for the elastic local buckling of the straight part of the composite CSP pipe-arch are derived. In the established mechanical model, a semi-combined state is a bonding condition between the upper and lower layers that lies between a fully smooth interface and a fully bonded state. The loaded edge of the straight part is assumed to be simply supported, while the unloaded edge is subject to elastic rotational restraint provided by the corrugated parts [56,57]. Soil support is represented as an elastic foundation that can only resist compression forces. Vertical tensile and compressive deformations, as well as horizontal shear deformations of the material cross-section, are considered negligible. The layers of the composite CSP pipe-arch are assumed to be vertically continuous, with isotropic material properties in both the cross-section and material. Through theoretical analysis and numerical solutions, it is determined that the critical buckling load and critical instability modes of the composite CSP pipe-arch are influenced by multiple parameters. Solutions for enhancing local buckling stability are also provided. Pure critical buckling analysis is crucial for understanding structural instability behavior. By determining the critical buckling load of a structure, it is possible to qualitatively predict the conditions under which instability may occur, serving as a key safety indicator in the design process. Although the pure critical buckling load does not represent the actual load-bearing capacity, it provides a foundation for further nonlinear analysis and design.

This paper is structured as follows. Section 2 establishes a theoretical mechanical model for composite CSP pipe-arch based on elastic stability theory, ring compression theory, and an approximate calculation method for the stiffness of semi-combined composite structures,

with the derivation of control equations. In Section 3, we compare the results with those from single-layer structures and finite element analysis. Section 4 explores the relationship between the stability of composite CSP pipe-arch and key parameters, including the effects on critical buckling wave number and load, as well as the impact of parameter coupling. Finally, Section 5 summarizes the research findings and presents the conclusions.

2. Theoretical Model and Formulation

This section constructs a theoretical mechanical model of composite CSP pipe-arch based on the theory of elastic stability [51] and the theory of ring compression [52]. The model includes the static characteristics of the composite CSP pipe-arch, the derivation of control equations, an approximate calculation method for the stiffness of semi-combined composite structures, the dimensionless formulation of system parameters, and the solution of variable coefficient control equations.

2.1. Modelling

As shown in Figure 3a, the composite CSP pipe-arch pipe-arch is buried in the soil. In pipe-arch structures, the lower section of the radius is typically quite large and can be approximated as a straight part with a span of a. The central part of each pipe-arch is hollow. In Figure 3b, the red cross-section of the composite CSP pipe-arch comprises two main parts: the corrugated part and the straight part. The symbols b, θ, and t denote the width of the straight part, the cut angle, and the thickness of the corrugated part, respectively. For a composite CSP pipe-arch with specific parameters, only the radius of the corrugated part can be determined. When the thickness is varied, the chamfering angle of the corrugated part and the width of the straight part will differ. To derive a general formula that applies to all corrugations and thicknesses, a local buckling analysis was conducted on the straight part of the invert in the composite CSP pipe-arch, with the assumption that the corrugated part provides elastic rotational constraints to the straight part [56,57]. Consequently, the straight part of the composite CSP pipe-arch can be considered a rectangular plate constrained by the corrugated part, as depicted in Figure 3c.

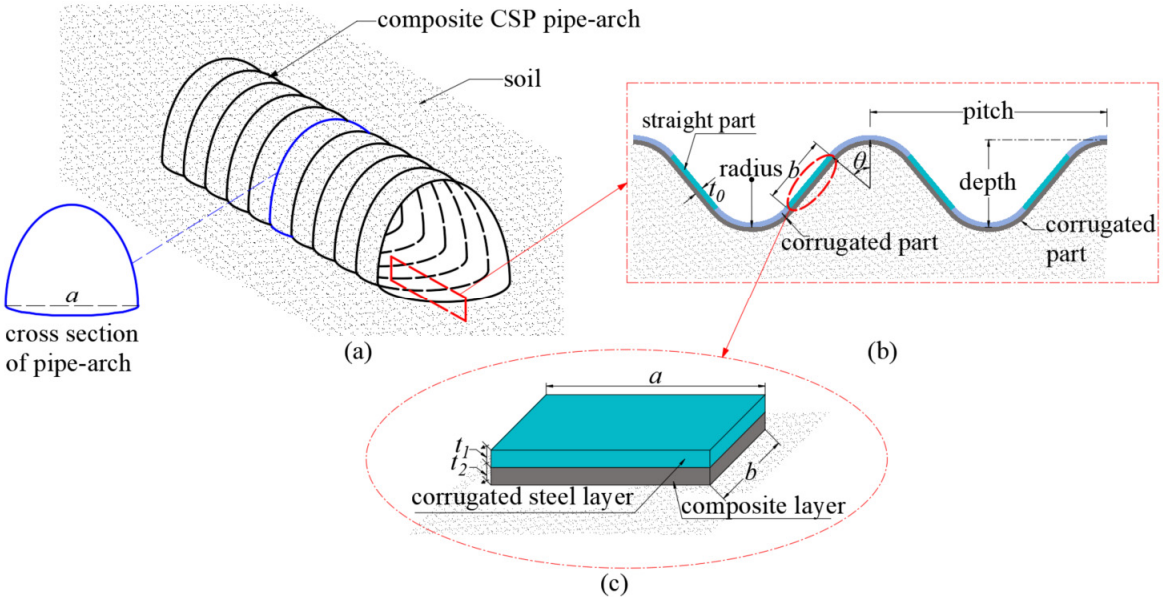


Figure 3. Diagram of CSP pipe-arch-based composite structure. (**a**) Embedded composite CSP pipe-arch; (**b**) Simplified structural diagram; (**c**) Schematic diagram of the straight part.

In Figure 4a, the length of the straight part is a, and the width of the straight part is b. According to the ring compression theory [55], the short side of the straight part is subject to a uniform compression force P_x in the y direction. It is assumed that the load edge of the

straight part is simply supported, and the unloading edge is subject to elastic rotational constraints with rotational constraint stiffness ξ [56]. Soil support is replaced by a series of springs in the normal direction of the composite structure to simulate the soil support that only bears compressive force.

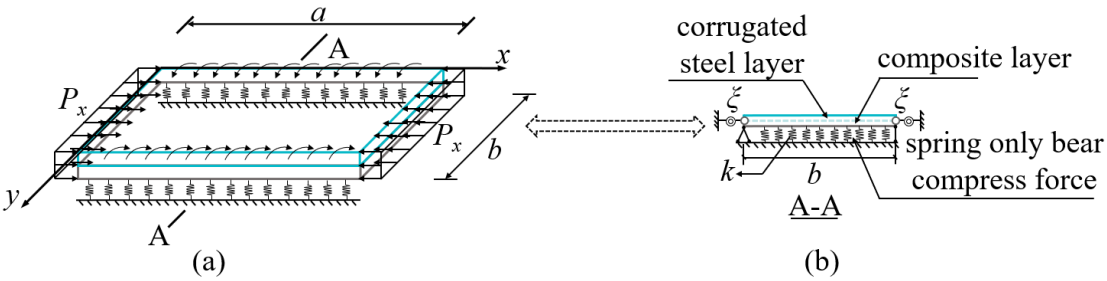


Figure 4. Schematic diagram of the mechanical model of the straight part of the composite CSP pipe-arch structure. (**a**) Schematic diagram of equivalent stress on the straight part of the composite structure; (**b**) Equivalent stress diagram of A-A section.

2.2. Governing Equations

According to the classical theory of elastic stability [54], when calculating the critical value of the forces acting on the mid-plane of the plate, the plane equilibrium form becomes unstable at this critical value. The differential equation governing the deflection surface of composite structure buckling plates is given by the following formula:

$$D\left(\frac{\partial^4 w}{\partial x^4}+2\frac{\partial^4 w}{\partial x^2\partial y^2}+\frac{\partial^4 w}{\partial y^4}\right)=P_x\frac{\partial^2 w}{\partial x^2}+2P_{xy}\frac{\partial^2 w}{\partial x\partial y}+P_y\frac{\partial^2 w}{\partial y^2}, \tag{1}$$

where P_x is the axial force per unit length in the x-axis direction of the straight part, P_y is the axial force per unit length in the y-axis direction of the straight part, and P_{xy} is the shear force per unit length on the cross section.

In this article, a composite CSP pipe-arch composed of two layers of materials is studied. The bending stiffness of the corrugated steel layer is

$$D_1=\frac{E_1t_1^3}{12(1-\mu_1^2)}, \tag{2}$$

where E_1 is the elastic modulus of the corrugated steel layer, t_1 is the thickness of the corrugated steel layer, and μ_1 is the Poisson's ratio.

The bending stiffness of the composite layer material is written as

$$D_2=\frac{E_2t_2^3}{12(1-\mu_2^2)}, \tag{3}$$

where E_2 is the elastic modulus of the composite layer, t_2 is the thickness of the composite layer, and μ_2 is the Poisson's ratio. Additionally, the composite layer mentioned here does not refer to any specific material; it can be selected based on actual needs, such as alloys, concrete, fireproof boards, or other functional materials, with no fixed range for its elastic modulus.

Considering that the composite CSP pipe-arch in this article is combined with double-layer plates, this article adopts a semi-combined composite structure stiffness approximate calculation method. A semi-combined state is a bonding condition between the upper and lower layers that lies between a fully smooth interface and a fully bonded state. The assumptions during the calculation process are: (1) The bending of the double-layer plate has a small deflection, that is, the vertical tension and compression and horizontal shear deformation of the plate section can be ignored; (2) The layers are vertically continuous,

and there is no voiding phenomenon; (3) The plates are of equal cross-section, and the material is isotropic.

As shown in Figure 5, when the layers of the composite CSP pipe-arch structure are smooth, the neutral planes of the upper and lower layers are located at their respective mid-planes, which correspond to the blue planes along the x_1 and x_2 axes in Figure 5b. When the layers are combined (that is, there is no horizontal displacement), the upper and lower layers have the same neutral plane (the red plane along the x0 axis, which is not the bonding surface between the upper and lower layers), and the distances between it and the middle of the upper and lower layers are t_s and t_d respectively. When the interlayer contact condition of the composite structure transitions from the smooth state to the bonded state, the neutral layers of the upper and lower layers transition from the x_1 and x_2 axes of the smooth state to the x_0 axis of the bonded state. Their distances from the x_1 and x_2 axes are $t_s\lambda$ and $t_d\lambda$, respectively, with $\lambda \in [0, 1]$. When $\lambda = 0$, the layers are in a smooth state. When $\lambda = 1$, the layers are in a bonded state. When $0 < \lambda < 1$, they are in a semi-combined state [58].

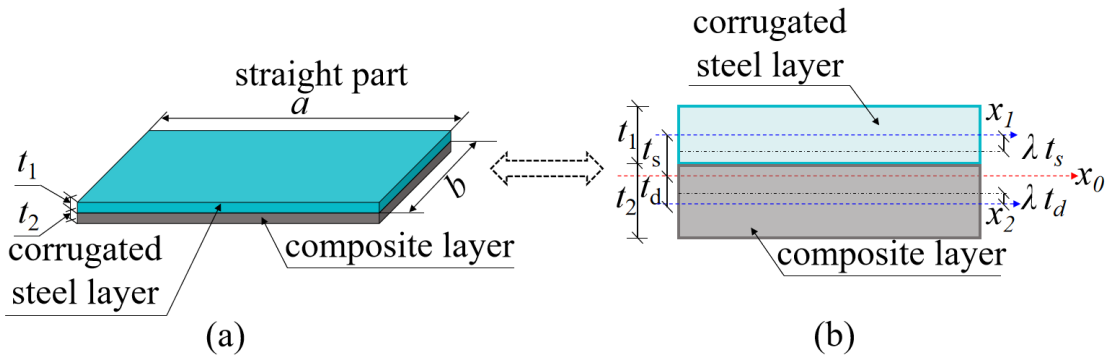


Figure 5. Graphical analysis of semi-combined composite structures. (**a**) Diagram of the straight part of CSP pipe-arch-based composite structure; (**b**) Semi-combined state schematic diagram.

The composite CSP pipe-arch structure primarily consists of an upper CSP pipe-arch combined with other materials in the lower layer. The interlayer bonding stiffness at the junction is a crucial factor influencing the stability of the structure. During the transition from a smooth state to a fully bonded state, the interlayer bonding stiffness between the upper and lower materials at different bonding states can be expressed as

$$D_3 = \tau\lambda t_0^2/4, \tag{4}$$

where $t_0 = t_1 + t_2$ is the total thickness of the composite CSP pipe-arch, $\tau = ((1-\mu_1^2)/E_1t_1 + (1-\mu_2^2)/E_2t_2)^{-1}$ is the relative compressive stiffness of the composite CSP pipe-arch, and λ is the inter-layer bonding coefficient of the composite CSP pipe-arch.

Since the Poisson's ratios of the upper and lower layer board materials are generally close, the difference between the two materials is ignored in this article, and the Poisson's ratio is uniformly recorded as μ in the following article.

Therefore, by combining Equations (2)–(4), the bending stiffness of the composite CSP pipe-arch can be obtained as D, denoted as

$$D = D_1 + D_2 + D_3. \tag{5}$$

The strain energy U_e of the composite CSP pipe-arch and the potential energy of the external force V are obtained from Equations (6) and (7):

$$U_e = \frac{D}{2}\int_0^a \int_0^b \left\{ \left(\frac{\partial^2 w}{\partial x^2} + \frac{\partial^2 w}{\partial y^2}\right)^2 - 2(1-\mu)\left[\frac{\partial^2 w}{\partial x^2}\frac{\partial^2 w}{\partial y^2} - \left(\frac{\partial^2 w}{\partial x \partial y}\right)^2\right]\right\} dxdy, \tag{6}$$

$$V = -\frac{1}{2}\int_0^a \int_0^b \left[P_x \left(\frac{\partial w}{\partial x}\right)^2 + P_y \left(\frac{\partial w}{\partial y}\right)^2 + 2P_{xy}\frac{\partial w}{\partial x}\frac{\partial w}{\partial y}\right] dxdy. \tag{7}$$

Considering the boundary conditions and deformation coordination requirements, it is assumed that the deformation function of the straight part in the x direction (long side) is a sinusoidal series, while in the y direction (short side), it is a fourth-order polynomial. Thus, the deformation function of the straight part can be expressed as follows:

$$w(x,y) = \left[\left(\frac{y}{b}\right) + \delta\left(\frac{y}{b}\right)^2 - 2(1+\delta)\left(\frac{y}{b}\right)^3 + (1+\delta)\left(\frac{y}{b}\right)^4 \right] \sum_{m=1}^{M} C_m \sin\frac{m\pi x}{a}. \tag{8}$$

The boundary conditions of the straight part of the composite CSP pipe-arch structure are obtained from Equation (9):

$$\begin{cases} w(x,y)|_{x=0} = 0, \quad \frac{\partial^2 w(x,y)}{\partial x^2}|_{x=0} = 0 \\ w(x,y)|_{x=a} = 0, \quad \frac{\partial^2 w(x,y)}{\partial x^2}|_{x=a} = 0 \\ -D\left(\frac{\partial^2 w(x,y)}{\partial y^2}|_{y=0}\right) = -\xi\left(\frac{\partial w(x,y)}{\partial y}|_{y=0}\right) \\ -D\left(\frac{\partial^2 w(x,y)}{\partial y^2}|_{y=b}\right) = \xi\left(\frac{\partial w(x,y)}{\partial y}|_{y=b}\right), \end{cases} \tag{9}$$

where m represents the buckling wave number of the straight part in the x direction, and only integer values of m are considered in the calculation process.

Substituting the boundary conditions from Equation (9) into Equation (8), the expression for the rotational restraint coefficient δ at the unloaded edge of the plane segment is derived from Equation (10):

$$\delta = \frac{\xi b}{2D}. \tag{10}$$

Substituting Equation (10) into Equation (8), Equation (8) can be further rewritten as Equation (11):

$$w(x,y) = \left[\frac{y}{b} + \frac{\xi}{2bD}y^2 - \frac{2D+\xi b}{Db^3}y^3 + \frac{2D+\xi b}{2Db^4}y^4 \right] \sum_{m=1}^{M} C_m \sin\frac{m\pi x}{a}. \tag{11}$$

2.3. Buckling for an Even Value of m

Considering that the soil can only withstand compressive forces, the soil provides restraint when the composite CSP pipe-arch contacts it. However, this restraint fails when the plate moves away from the soil. Therefore, when m is an odd or even number, the relevant formulas for the local buckling of the straight part should be derived separately. Using the Rayleigh–Ritz method, the total potential energy Λ is expressed as the sum of the strain energy and the potential energy of the external forces.

When the buckling wave number is even, Λ can be expressed as

$$\Lambda = \frac{1}{2}U_k + U_e + U_\xi + V, \tag{12}$$

where U_e and V can be determined by Equations (6) and (7), and the elastic potential energy U_ξ of the rotation constraint boundary and the elastic potential energy U_k of the elastic foundation can be obtained by Equations (13) and (14).

$$U_\xi = \frac{\xi}{2}\int_0^a \left[\left(\frac{\partial w}{\partial y}|_{y=0}\right)^2 + \left(\frac{\partial w}{\partial y}|_{y=b}\right)^2 \right] dx, \tag{13}$$

$$U_k = \frac{1}{2}\int_0^a \int_0^b k w^2(x,y) dxdy. \tag{14}$$

Therefore, Equations (6), (7), (13) and (14) are simultaneously expressed, and Equation (12) can be rewritten as Equation (15):

$$\Lambda = \frac{1}{2}T_1 abk\sum_{m=1}^{M} C_m^2 + \frac{D}{2}\left[\frac{\pi^4 bT_3\sum_{m=1}^{M} m^4 C_m^2}{a^3} + \frac{aT_4\sum_{m=1}^{M} C_m^2}{b^3} + \frac{\pi^2(T_5-\mu T_6)\sum_{m=1}^{M}(mC_m)^2}{ab}\right] + \frac{\xi a\left(1+T_2^2\right)\sum_{m=1}^{M} C_m^2}{4b^2}U_\xi - \frac{T_1 P_x \pi^2 b\sum_{m=1}^{M}(mC_m)^2}{a}, \tag{15}$$

where T_1, T_2, T_3, T_4, T_5 and T_6 are

$$\begin{cases} T_1 = \frac{1}{2520}\delta^2 + \frac{11}{2520}\delta + \frac{31}{2520} \\ T_2 = -1 \\ T_3 = \frac{1}{1260}\delta^2 + \frac{11}{1260}\delta + \frac{31}{1260} \\ T_4 = \frac{2}{5}\delta^2 + \frac{4}{5}\delta + \frac{12}{5} \\ T_5 = \frac{2}{105}\delta^2 + \frac{6}{35}\delta + \frac{17}{35} \\ T_6 = 0 \end{cases}. \tag{16}$$

According to the principle of minimum potential energy, by substituting Equation (16) into the relevant expression $\partial\Lambda/\partial C_m = 0$, the local buckling load $P_{x_cr}^m$ can be determined using Equation (17):

$$P_{x_cr}^m = \kappa\frac{D\pi^2}{b^2}, \tag{17}$$

among them, the buckling coefficient κ can be determined by Equation (18):

$$\kappa = \frac{\eta^2(1+T_2^2)\delta}{2\pi^4 m^2 T_1} + \frac{T_3 m^2}{2\eta^2 T_1} + \frac{T_4\eta^2}{2\pi^4 m^2 T_1} + \frac{(T_5-\mu T_6)}{2\pi^2 T_1} + \frac{a^4 k}{2Dm^2\eta^2\pi^4}, \tag{18}$$

where η is the aspect ratio of the straight part, which is defined as $\eta = a/b$.

Therefore, by substituting Equation (18) into Equation (17), the local buckling load $P_{x_cr}^m$ can be rewritten as

$$P_{x_cr}^m = \left(\frac{\eta^2(1+T_2^2)\delta}{2\pi^4 m^2 T_1} + \frac{T_3 m^2}{2\eta^2 T_1} + \frac{T_4\eta^2}{2\pi^4 m^2 T_1} + \frac{(T_5-\mu T_6)}{2\pi^2 T_1} + \frac{a^4 k}{2Dm^2\eta^2\pi^4}\right)\frac{D\pi^2}{b^2}. \tag{19}$$

When $\partial\kappa/\partial m = 0$, the critical buckling coefficient κ can be obtained. By substituting Equation (18) into $\partial\kappa/\partial m = 0$, the calculation formula of the even critical buckling wave number can be obtained:

$$\frac{T_3 m^4}{\eta^2 T_1} - \frac{\eta^2(1+T_2^2)\delta + T_4\eta^2}{\pi^4 T_1} - \frac{a^4 k}{D\eta^2\pi^4} = 0. \tag{20}$$

Then, the critical buckling wave number m_{cr} calculated by Equation (20) is substituted into Equations (18) and (19), and the critical buckling coefficient κ_{cr} and critical buckling load P_{x_cr} corresponding to the even critical buckling wave number can be obtained.

2.4. Buckling for an Odd Value of m

When the buckling wave number is odd, Λ can be expressed as

$$\Lambda = \gamma U_k + U_e + U_\xi + V, \tag{21}$$

where, considering the support effect of the soil, γ can be expressed as:

$$\gamma = \frac{m-1}{2m} \text{ or } \gamma = \frac{m+1}{2m}. \tag{22}$$

Based on the principle of minimum potential energy, the buckling coefficient κ for odd buckling wave number can be determined using the following equation.

$$\kappa = \frac{\eta^2(1+T_2^2)\delta}{2\pi^4 m^2 T_1} + \frac{T_3 m^2}{2\eta^2 T_1} + \frac{T_4\eta^2}{2\pi^4 m^2 T_1} + \frac{(T_5 - \mu T_6)}{2\pi^2 T_1} + \frac{a^4 k\gamma}{Dm^2\eta^2\pi^4}. \tag{23}$$

Therefore, the local buckling load $P_{x_cr}^m$ for odd buckling wave number can be rewritten as

$$P_{x_cr}^m = \left(\frac{\eta^2(1+T_2^2)\delta}{2\pi^4 m^2 T_1} + \frac{T_3 m^2}{2\eta^2 T_1} + \frac{T_4\eta^2}{2\pi^4 m^2 T_1} + \frac{(T_5 - \mu T_6)}{2\pi^2 T_1} + \frac{a^4 k\gamma}{Dm^2\eta^2\pi^4} \right) \frac{D\pi^2}{b^2}. \tag{24}$$

When $\partial\kappa/\partial m = 0$, the critical buckling coefficient κ can be obtained. By substituting Equation (23) into $\partial\kappa/\partial m = 0$, an odd critical buckling wave number can be obtained.

When $\gamma = (m-1)/2m$, the odd critical buckling wave number is obtained from Equation (25):

$$\frac{T_3 m^5}{\eta^2 T_1} + \frac{3a^4 k}{2D\pi^4\eta^2} - m\frac{\eta^2(1+T_2^2)\delta + \eta^2 T_4}{T_1\pi^4} - \frac{ma^4 k}{\eta^2 D\pi^4} = 0. \tag{25}$$

When $\gamma = (m+1)/2m$, the odd critical buckling wave number is obtained from Equation (26):

$$\frac{T_3 m^5}{\eta^2 T_1} - \frac{3a^4 k}{2D\pi^4\eta^2} - m\frac{\eta^2(1+T_2^2)\delta + \eta^2 T_4}{T_1\pi^4} - \frac{ma^4 k}{\eta^2 D\pi^4} = 0. \tag{26}$$

Then, the critical buckling wave number m_{cr} calculated by Equation (25) or Equation (26) is substituted into Equations (23) and (24), and the critical buckling coefficient κ_{cr} and critical buckling load P_{x_cr} corresponding to the odd critical buckling wave number can be obtained.

2.5. Nondimensionation and Solution Method

To nondimensionalize the governing equations above, we introduce the following dimensionless parameters: $\overline{b} = b/a$, $\overline{t}_1 = t_1/a$, $\overline{t}_2 = t_2/a$, $\overline{E}_2 = E_2/E_1$, $\overline{\xi} = \xi/ka^3$, $\overline{D}_1 = D_1/ka^4$, $\overline{D}_2 = D_2/ka^4$, and $D_3 = (\overline{\tau}\overline{t}_0^2\lambda)/4$. Here, $\overline{b}$ is the width of the straight part after dimensionless, $\overline{t}_1$ is the thickness of the corrugated steel layer after dimensionless, $\overline{t_2}$ is the thickness of the composite layer after dimensionless, $\overline{E}_2$ is the elastic modulus of the composite layer after dimensionless, $\overline{\xi}$ is the rotational constraint stiffness after dimensionless, $\overline{D}_1$ is the stiffness of corrugated steel layer after dimensionless, $\overline{D}_2$ is the dimensionless c composite layer stiffness, and $\overline{D}_3$ is the dimensionless rear combined bending stiffness.

Therefore, by combining Equations (2)–(4) and substituting the dimensionless parameters, Equation (5) can be rewritten as:

$$\overline{D} = \frac{\overline{t}_1^3}{12(1-\mu^2)} + \frac{\overline{E}_2\overline{t}_2^3}{12(1-\mu^2)} + \frac{1}{4}\frac{\overline{E}_2\overline{t}_1\overline{t}_2}{(1-\mu^2)(\overline{E}_2\overline{t}_2 + \overline{t}_1)}(\overline{t}_1 + \overline{t}_2)^2. \tag{27}$$

Substituting Equation (5), the dimensionless rotational constraint stiffness $\overline{\xi}$ and the width $\overline{b}$ of the straight part into Equation (10), the dimensionless parameter rotational constraint coefficient can be obtained:

$$\overline{\delta} = \overline{\xi}\overline{b}/2\overline{D}. \tag{28}$$

Therefore, the dimensionless Equation (16) is derived from the following formula:

$$\begin{cases} \overline{T}_1 = \frac{1}{2520}\overline{\delta}^2 + \frac{11}{2520}\overline{\delta} + \frac{31}{2520} \\ \overline{T}_2 = -1 \\ \overline{T}_3 = \frac{1}{1260}\overline{\delta}^2 + \frac{11}{1260}\overline{\delta} + \frac{31}{1260} \\ \overline{T}_4 = \frac{2}{5}\overline{\delta}^2 + \frac{4}{5}\overline{\delta} + \frac{12}{5} \\ \overline{T}_5 = \frac{2}{105}\overline{\delta}^2 + \frac{6}{35}\overline{\delta} + \frac{17}{35} \\ \overline{T}_6 = 0 \end{cases}. \tag{29}$$

Simultaneously, combining Equations (27)–(29) and substituting the dimensionless parameters into Equations (18) and (19), when the buckling wave number is an even number, the dimensionless buckling coefficient $\overline{\kappa}$ and the dimensionless local buckling load $\overline{P}^m_{x_cr}$ are:

$$\overline{\kappa} = \frac{\overline{\eta}^2(1+\overline{T}_2^2)\overline{\delta}}{2\pi^4 m^2 \overline{T}_1} + \frac{\overline{T}_3 m^2}{2\overline{\eta}^2\overline{T}_1} + \frac{\overline{T}_4\overline{\eta}^2}{2\pi^4 m^2\overline{T}_1} + \frac{(\overline{T}_5 - \mu\overline{T}_6)}{2\pi^2\overline{T}_1} + \frac{1}{2\overline{D}m^2\overline{\eta}^2\pi^4}, \tag{30}$$

$$\overline{P}^m_{x_cr} = \left(\frac{\overline{\eta}^2(1+\overline{T}_2^2)\overline{\delta}}{2\pi^4 m^2 \overline{T}_1} + \frac{\overline{T}_3 m^2}{2\overline{\eta}^2\overline{T}_1} + \frac{\overline{T}_4\overline{\eta}^2}{2\pi^4 m^2\overline{T}_1} + \frac{(\overline{T}_5 - \mu\overline{T}_6)}{2\pi^2\overline{T}_1} + \frac{1}{2\overline{D}m^2\overline{\eta}^2\pi^4}\right)\frac{\overline{D}\pi^2}{\overline{b}^2}, \tag{31}$$

where the aspect ratio of the straight part is $\overline{\eta} = 1/\overline{b}$.

The dimensionless calculation formula of even critical buckling wave number is obtained from Equation (32)

$$\frac{\overline{T}_3 m^4}{\overline{\eta}^2\overline{T}_1} - \frac{\overline{\eta}^2(1+\overline{T}_2^2)\overline{\delta} + \overline{T}_4\overline{\eta}^2}{\pi^4\overline{T}_1} - \frac{1}{\overline{D}\overline{\eta}^2\pi^4} = 0. \tag{32}$$

In the same way, when the buckling wave number is odd, the dimensionless buckling coefficient $\overline{\kappa}$ and the local buckling load $\overline{P}^m_{x_cr}$ are

$$\overline{\kappa} = \frac{\overline{\eta}^2(1+\overline{T}_2^2)\overline{\delta}}{2\pi^4 m^2 \overline{T}_1} + \frac{\overline{T}_3 m^2}{2\overline{\eta}^2\overline{T}_1} + \frac{\overline{T}_4\overline{\eta}^2}{2\pi^4 m^2\overline{T}_1} + \frac{(\overline{T}_5 - \mu\overline{T}_6)}{2\pi^2\overline{T}_1} + \frac{\gamma}{\overline{D}m^2\overline{\eta}^2\pi^4}, \tag{33}$$

$$\overline{P}^m_{x_cr} = \left(\frac{\overline{\eta}^2(1+\overline{T}_2^2)\overline{\delta}}{2\pi^4 m^2 \overline{T}_1} + \frac{\overline{T}_3 m^2}{2\overline{\eta}^2\overline{T}_1} + \frac{\overline{T}_4\overline{\eta}^2}{2\pi^4 m^2\overline{T}_1} + \frac{(\overline{T}_5 - \mu\overline{T}_6)}{2\pi^2\overline{T}_1} + \frac{\gamma}{\overline{D}m^2\overline{\eta}^2\pi^4}\right)\frac{\overline{D}\pi^2}{\overline{b}^2}, \tag{34}$$

where, when $\gamma = (m-1)/2m$, the odd critical buckling wave number is given by Equation (35):

$$\frac{\overline{T}_3 m^5}{\overline{\eta}^2\overline{T}_1} + \frac{3}{2\overline{D}\pi^4\overline{\eta}^2} - m\frac{\overline{\eta}^2(1+\overline{T}_2^2)\overline{\delta} + \overline{\eta}^2\overline{T}_4}{\overline{T}_1\pi^4} - \frac{m}{\overline{\eta}^2\overline{D}\pi^4} = 0, \tag{35}$$

when $\gamma = (m+1)/2m$, the odd critical buckling wave number is given by Equation (36):

$$\frac{\overline{T}_3 m^5}{\overline{\eta}^2\overline{T}_1} - \frac{3}{2\overline{D}\pi^4\overline{\eta}^2} - m\frac{\overline{\eta}^2(1+\overline{T}_2^2)\overline{\delta} + \overline{\eta}^2\overline{T}_4}{\overline{T}_1\pi^4} - \frac{m}{\overline{\eta}^2\overline{D}\pi^4} = 0. \tag{36}$$

By giving the dimensionless parameters $\overline{b}$, $\overline{E}_2$, $\overline{t}_1$, $\overline{t_2}$, λ, μ, and $\overline{\xi}$, the solutions of Equations (27)–(36) can be numerically obtained by programming in the Matlab R2016b software. By substituting the dimensionless related parameters into Equations (27)–(29), the related intermediate quantities are calculated, and then the calculated intermediate quantities are substituted into Equations (30) and (32) to obtain the dimensionless buckling coefficient and the even critical buckling wave number, and then substituted into Equation (31) to obtain the critical local buckling load under the condition of the even critical buckling wave number. Similarly, by substituting the calculated intermediate quantities into Equations (33), (35) or (36), the dimensionless buckling coefficient and the odd critical buckling wave number are obtained and then substituted into Equation (34) to obtain the local buckling load under the condition of the odd critical buckling wave number.

3. Comparison and Validation

In this section, we first degrade the composite CSP pipe-arch to a "single-layer" CSP pipe-arch and compare its critical buckling load analytical solution with that of the existing single-layer CSP pipe-arch. We analyze the differences in local stability between the two and use finite element analysis to verify the reliability of the local stability calculation method proposed in this study.

3.1. Comparison with Analytical Solution of Single-Layer Structure

In this paper, in order to study the local stability performance of composite CSP pipe-arch, a corresponding estimation of the dimensionless parameters is required. The critical conditions of composite CSP pipe-arch are analyzed based on dimensionless typical values. From previous experiments, the material properties and geometric parameters can be obtained, as shown in Table 1. The critical conditions of the composite CSP pipe-arch are numerically analyzed using the dimensionless typical values in Table 2 as a reference.

Table 1. Material Properties and Geometric Parameters.

Parameter	Definition	Value	Units
a	Length of the straight part	5×10^2~30×10^2	mm
b	Width of the straight part	30~60	mm
E_1	Elastic modulus of corrugated steel layer	2.0×10^{11}~2.1×10^{11}	N/m^2
E_2	Elastic modulus of the composite layer	4.0×10^9~2.0×10^{11}	N/m^2
t_1	Thickness of the corrugated steel layer	1~3	mm
t_2	Thickness of the composite layer	1~3	mm
λ	Inter-layer bonding coefficient	0–1	/
μ	Poisson's ratio	0–0.6	/
ξ	Rotational restraint stiffness	10~9.9×10^3	N/rad
k	Soil compression stiffness	1.4×10^7~6.5×10^7	N/m^3

Table 2. Dimensionless Parameters.

Parameter	$\overline{b}$	$\overline{E}_2$	$\overline{t}_1$	$\overline{t}_2$	λ	μ	$\overline{\xi}$
Value	0.1–0.5	0.02–1	0.01–0.03	0.01–0.03	0–1	0–0.6	0.05–1

By setting $\overline{E}_2 = 1$ and $\lambda = 1$, the upper and lower layer materials are identical, and the composite CSP pipe-arch can be regarded as a fully bonded continuum, then the composite CSP pipe-arch transforms into a "single-layer" CSP pipe-arch structure. It can be seen from Figure 6 that the critical local buckling load increases with the increase in thickness, whether it is a single-layer CSP pipe-arch or a composite CSP pipe-arch. In addition, when the total thickness t is the same, the critical buckling load of the composite CSP pipe-arch is improved to a certain extent compared with the single-layer CSP pipe-arch. Therefore, it can be found that when the total thickness is constant, the use of composite CSP pipe-arch has higher local stability.

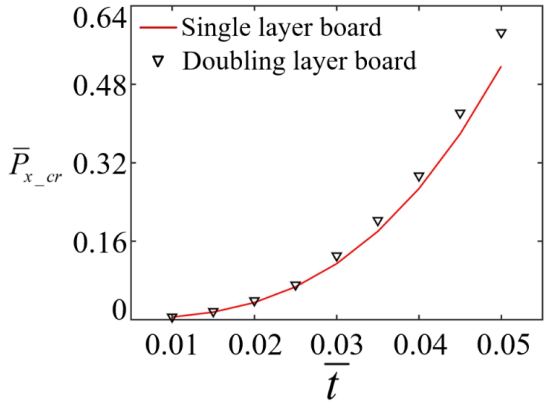


Figure 6. Comparison between the two critical local buckling loads obtained from composite CSP pipe-arch theory and single-layer CSP pipe-arch theory [15] as a function of thickness for $\overline{b} = 0.24$, $\overline{E}_2 = 1$, $\lambda = 1$, $\mu = 0.3$ and $\overline{\xi} = 0.5$.

3.2. Comparison with Finite Element Results

Figure 7 clearly shows that the numerical curve of the analytical solution closely matches the finite element analysis results, confirming the reliability of the local stability calculation method for the composite CSP pipe-arch structure presented in this article.

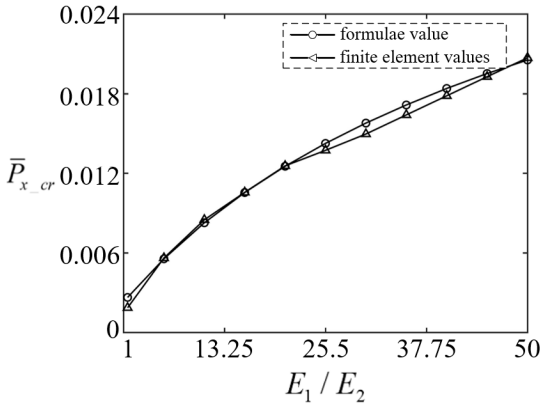


Figure 7. Comparison of critical buckling load as a function of elastic modulus between analytical solution and finite element analysis results of composite CSP pipe-arch.

4. Bucking Behaviors

By solving the above governing equations, it is found that the local buckling stability conditions of the composite CSP pipe-arch are related to the following parameters: $\overline{b}$, $\overline{E}_2$, $\overline{t}_1$, $\overline{t}_2$, λ, μ, and $\overline{\xi}$. This section will discuss the specific effects of these individual parameters on the local buckling stability of the composite CSP pipe-arch and present the variations in critical buckling load and critical buckling wave number with respect to each parameter. Additionally, considering that $\overline{b}$, $\overline{t}_1$, and $\overline{\xi}$ are all related to the plate's transverse bending stiffness, the coupling effects between these parameters on the critical buckling load are also discussed in order to guide the application in actual engineering.

4.1. Effect of the Width of the Straight Part

In the calculation, we give the dimensionless parameters $\overline{E}_2 = 1$, $\overline{t}_1 = 0.015$, $\overline{t}_2 = 0.012$, $\lambda = 1$, $\mu = 0.3$ and $\overline{\xi} = 0.5$. It can be seen from Figure 8a that the dimensionless critical buckling wave number $\overline{m}_{cr}$ gradually decreases as the dimensionless width $\overline{b}$ increases, and it can also be concluded that as the dimensionless width $\overline{b}$ increases, the dimensionless critical buckling load $\overline{p}_{x_cr}$ gradually decreases. The above results are that as the width of the straight part increases, the corrugation depth of the CSP pipe-arch becomes larger,

causing the CSP pipe-arch to be easily unstable; therefore, the wave number drops sharply in Figure 8a. Conversely, a relatively smaller width enhances the stability of the CSP pipe-arch, thereby resulting in larger critical buckling wave numbers and critical buckling loads upon instability. In practical engineering applications, selecting a relatively smaller width of the straight part can yield improved stability.

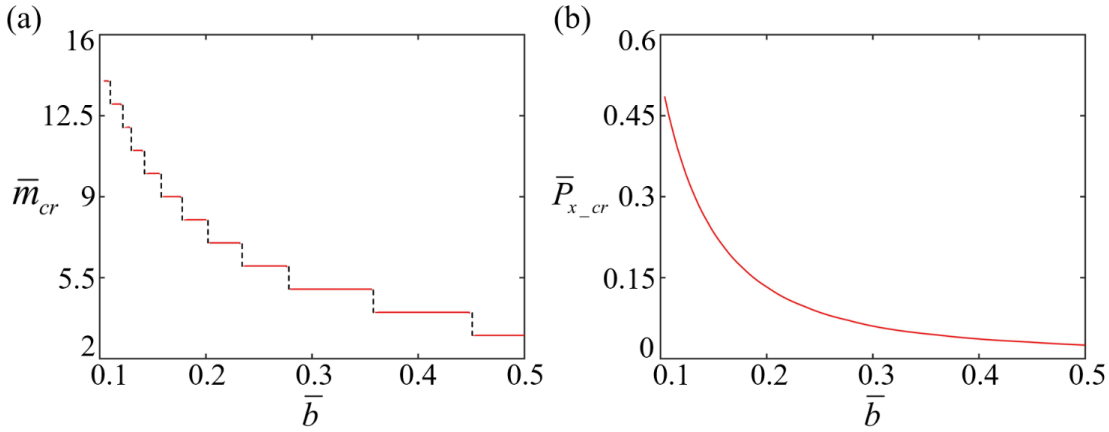


Figure 8. Effect of the width $\overline{b}$ of the straight part on critical buckling load $\overline{P}_{x_cr}$ and critical buckling wave number $\overline{m}_{cr}$ for $\overline{E}_2 = 1$, $\overline{t}_1 = 0.015$, $\overline{t}_2 = 0.012$, $\lambda = 1$, $\mu = 0.3$ and $\overline{\xi} = 0.5$. (**a**) Dependence of the dimensionless critical buckling wave number $\overline{m}_{cr}$ on the dimensionless width $\overline{b}$ of the straight part. (**b**) Dependence of the dimensionless critical buckling load $\overline{P}_{x_cr}$ on the dimensionless width $\overline{b}$ of the straight part.

4.2. Effect of the Elastic Modulus of the Composite Layer

In the calculation, we give the dimensionless parameters $\overline{b} = 0.24$, $\overline{t}_1 = 0.015$, $\overline{t}_2 = 0.012$, $\lambda = 1$, $\mu = 0.3$ and $\overline{\xi} = 0.5$. According to Figure 9, by altering the elastic modulus of the composite layer, we observe as the elastic modulus of the composite layer increases, the critical buckling wave number experiences a jump decrease from an odd to an even wave number while the critical buckling load gradually increases. The rationale behind this phenomenon remains the same as before: the increase in the elastic modulus of the composite layer enhances the overall stiffness of the composite CSP pipe-arch, thereby increasing its strength. As a result, a higher load is required to induce instability; moreover, the increase in the stiffness of the composite CSP pipe-arch leads to an increase in the wavelength at instability, resulting in a decrease in the wave number.

The dimensionless elastic modulus $\overline{E}_2$ of the composite layer is defined as the ratio of the composite layer's elastic modulus E_2 to the corrugated steel layer's elastic modulus E_1. Since E_1 for steel typically does not vary significantly, this primarily reflects changes in the composite layer's material. A higher elastic modulus in the composite layer increases the stiffness of the composite CSP pipe-arch, enhancing structural stability. The range of the elastic modulus E_2 provided in this paper is solely for the convenience of theoretical analysis and is not specific to any particular material. Instead, it can be selected based on actual needs, such as alloys, concrete, fireproof panels, or other functional materials. Therefore, choosing materials with a higher elastic modulus according to application requirements can be an effective strategy to improve structural stability in engineering applications.

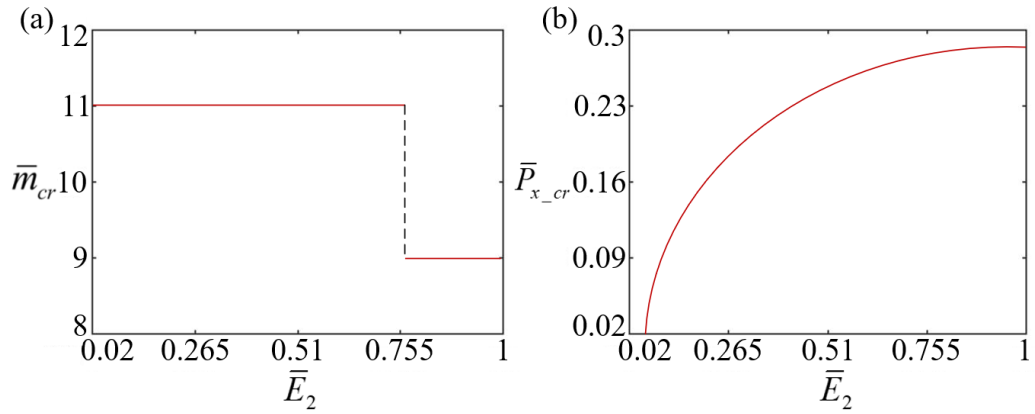


Figure 9. Effect of the dimensionless elastic modulus $\overline{E}_2$ of the composite layer on dimensionless critical buckling load $\overline{P}_{x_cr}$ and dimensionless critical buckling wave number $\overline{m}_{cr}$ for $\overline{b} = 0.24$, $\overline{t}_1 = 0.015$, $\overline{t}_2 = 0.012$, $\lambda = 1$, $\mu = 0.3$ and $\overline{\xi} = 0.5$. (**a**) Dependence of the dimensionless critical buckling wave number $\overline{m}_{cr}$ on the dimensionless elastic modulus $\overline{E}_2$ of the composite layer. (**b**) Dependence of the dimensionless critical buckling load $\overline{P}_{x_cr}$ on the elastic modulus of $\overline{E}_2$ the composite layer.

4.3. Effect of the Thickness of Corrugated Steel Layer

In the calculation, we give the dimensionless parameters $\overline{b} = 0.24$, $\overline{E}_2 = 1$, $\overline{t}_2 = 0.012$, $\lambda = 1$, $\mu = 0.3$ and $\overline{\xi} = 0.5$. As depicted in Figure 10a, within the given range of dimensionless parameters, the critical buckling wave number remains unchanged with an increase in the thickness of the corrugated steel layer. However, as inferred from Figure 10b, the critical buckling load increases with the increasing thickness of the corrugated steel layer. This phenomenon can be attributed to the fact that the increase in the thickness of the corrugated steel layer leads to an increase in the overall thickness of the composite CSP pipe-arch structure, thereby enhancing the stiffness of the composite structure. Consequently, a higher load is required to bring the composite CSP pipe-arch to its critical state of instability, resulting in a gradual increase in the critical buckling load. Nonetheless, the critical wave number of this structure at the point of instability does not change, which may be due to the changes in thickness within this numerical range not affecting the wavelength of the CSP pipe-arch at instability, thereby leaving the wave number unchanged.

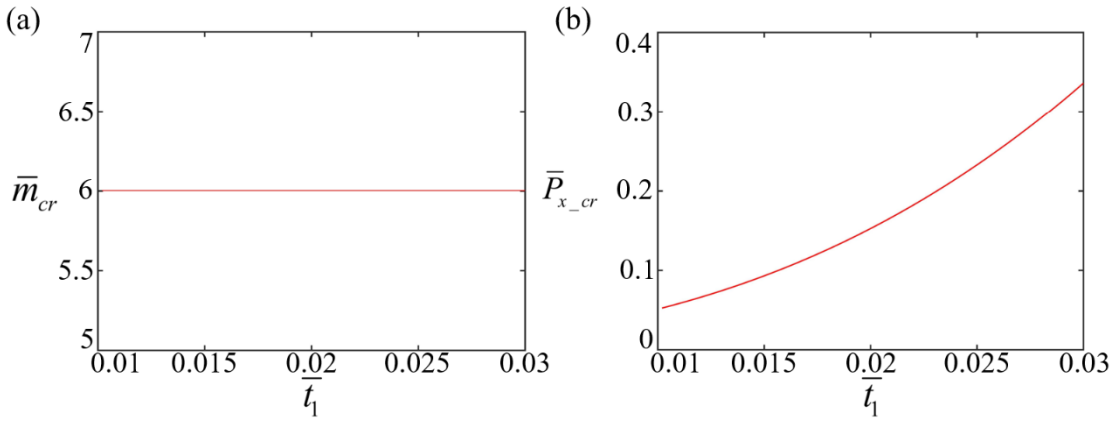


Figure 10. Effect of the dimensionless thickness $\overline{t}_1$ of corrugated steel layer on dimensionless critical buckling load $\overline{P}_{x_cr}$ and dimensionless critical buckling wave number $\overline{m}_{cr}$ for $\overline{b} = 0.24$, $\overline{E}_2 = 1$, $\overline{t}_2 = 0.012$, $\lambda = 1$, $\mu = 0.3$ and $\overline{\xi} = 0.5$. (**a**) Dependence of the dimensionless critical buckling wave number $\overline{m}_{cr}$ on the thickness $\overline{t}_1$ of corrugated steel layer. (**b**) Dependence of the dimensionless critical buckling load $\overline{P}_{x_cr}$ on the dimensionless thickness $\overline{t}_1$ of corrugated steel layer.

4.4. Effect of the Thickness of the Composite Layer

In the calculation, we give the dimensionless parameters $\overline{b} = 0.24$, $\overline{E}_2 = 1$, $\overline{t}_1 = 0.015$, $\lambda = 1$, $\mu = 0.3$ and $\overline{\xi} = 0.5$. By altering the thickness of the composite layer, we observe a similar pattern of change as depicted in Figure 10: within the specified range of dimensionless parameters, the critical buckling wave number remains unchanged with an increase in the thickness of the composite layer, while the critical buckling load gradually increases. The critical wave number of the composite CSP pipe-arch remains unchanged at the point of instability, possibly due to the thickness changes within this numerical range not significantly affecting the wavelength of the CSP pipe-arch at instability, resulting in no variation in the critical wave number. However, the increase in the thickness of the composite layer leads to an increase in the overall thickness of the composite CSP pipe-arch, which enhances the stiffness of the composite structure. Consequently, a higher load is required to reach the critical state of instability of the composite CSP pipe-arch structure, leading to a gradual increase in the critical buckling load.

From Figures 10 and 11, it is evident that changes in the thickness of any material within the composite structure have a significant impact on the instability behavior of the composite CSP pipe-arch structure. An increase in material thickness leads to greater stiffness of the composite CSP pipe-arch structure, implying enhanced stability. Therefore, in actual engineering applications, the thickness of the structure can be appropriately increased if conditions permit it to improve its stability.

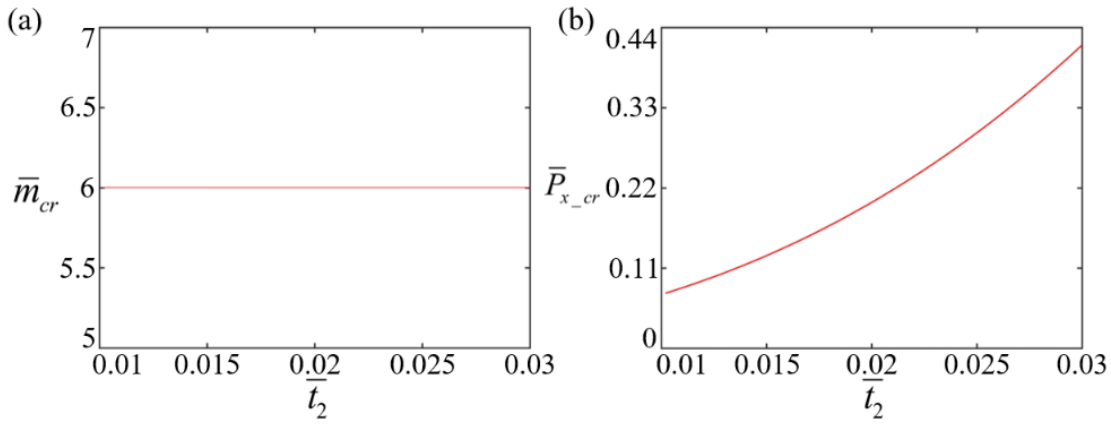


Figure 11. Effect of the dimensionless thickness $\overline{t}_2$ of the composite layer on dimensionless critical buckling load $\overline{P}_{x_cr}$ and critical buckling wave number $\overline{m}_{cr}$ for $\overline{b} = 0.24$, $\overline{E}_2 = 1$, $\overline{t}_1 = 0.015$, $\lambda = 1$, $\mu = 0.3$ and $\overline{\xi} = 0.5$. (**a**) Dependence of the dimensionless critical buckling wave number $\overline{m}_{cr}$ on the dimensionless thickness $\overline{t}_2$ of the composite layer. (**b**) Dependence of the dimensionless critical buckling load $\overline{P}_{x_cr}$ on the dimensionless thickness $\overline{t}_2$ of the composite layer.

4.5. Effect of the Inter-Layer Bonding Coefficient

In the calculation, we give the dimensionless parameters $\overline{b} = 0.24$, $\overline{E}_2 = 1$, $\overline{t}_1 = 0.015$, $\overline{t}_2 = 0.012$, $\mu = 0.3$ and $\overline{\xi} = 0.5$. As depicted in Figure 12a, within the given range of dimensionless parameters, the dimensionless critical buckling wave number $\overline{m}_{cr}$ decreases with an increase in the inter-layer bonding coefficient λ when the latter varies from 0 to 1. Conversely, as illustrated in Figure 12b, the dimensionless critical buckling load $\overline{P}_{x_cr}$ exhibits a linear increasing trend with the rise in the inter-layer bonding coefficient λ. The above results indicate that as the inter-layer bonding coefficient varies from 0 to 1, the composite CSP pipe-arch structure transitions from a state of mutual sliding between the two layers to a bonded state. This transition increases the material parameters such as thickness and stiffness of the composite CSP pipe-arch, thereby enhancing the structural stability. Consequently, the load required for buckling increases, leading to a gradual increase in the critical buckling load. Furthermore, the improvement in stability results in

an increase in the wavelength of the structure at buckling, causing a corresponding abrupt decrease in the wave number.

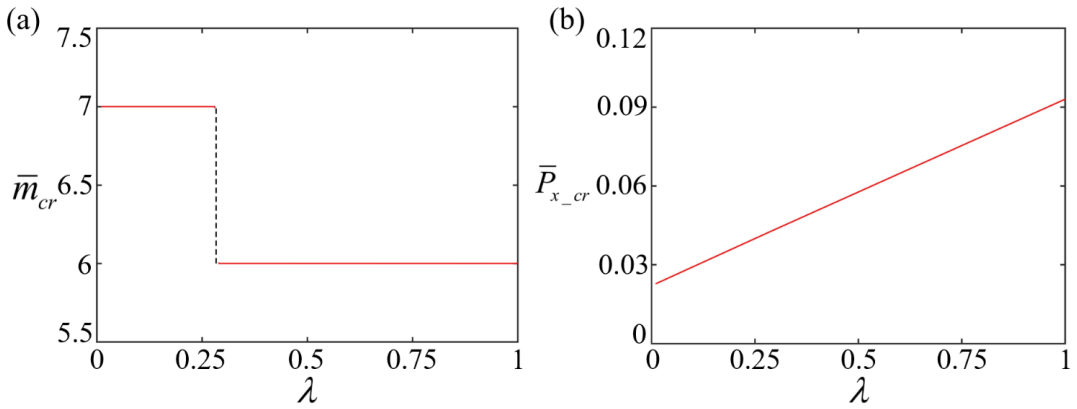


Figure 12. Effect of the inter-layer bonding coefficient λ on dimensionless critical buckling load $\overline{P}_{x_cr}$ and dimensionless critical buckling wave number $\overline{m}_{cr}$ for $\overline{b} = 0.24$, $\overline{E}_2 = 1$, $\overline{t}_1 = 0.015$, $\overline{t}_2 = 0.012$, $\mu = 0.3$ and $\overline{\xi} = 0.5$. (**a**) Dependence of the dimensionless critical buckling wave number $\overline{m}_{cr}$ on the inter-layer bonding coefficient k_u. (**b**) Dependence of the dimensionless critical buckling load $\overline{P}_{x_cr}$ on the inter-layer bonding coefficient λ.

4.6. Effect of the Poisson's Ratio

In the calculation, we give the dimensionless parameters $\overline{b} = 0.24$, $\overline{E}_2 = 1$, $\overline{t}_1 = 0.015$, $\overline{t}_2 = 0.012$, $\lambda = 1$ and $\overline{\xi} = 0.5$. As shown in Figure 13a, within the given range of dimensionless parameters, the critical buckling wave number $\overline{m}_{cr}$ remains constant as the Poisson's ratio μ increases. In contrast, Figure 13b reveals that the critical buckling load $\overline{P}_{x_cr}$ increases with an increase in the Poisson's ratio μ. This is because the increase in Poisson's ratio enhances the overall stiffness of the composite CSP pipe-arch, thereby improving the strength of the composite structure. Consequently, a higher load is required to bring the composite CSP pipe-arch to its critical buckling state, leading to a gradual increase in the critical buckling load. However, the critical wave number at buckling remains unchanged, possibly because the wavelength of the composite CSP pipe-arch at buckling does not vary within the given range of Poisson's ratio values, resulting in no change in the critical wave number.

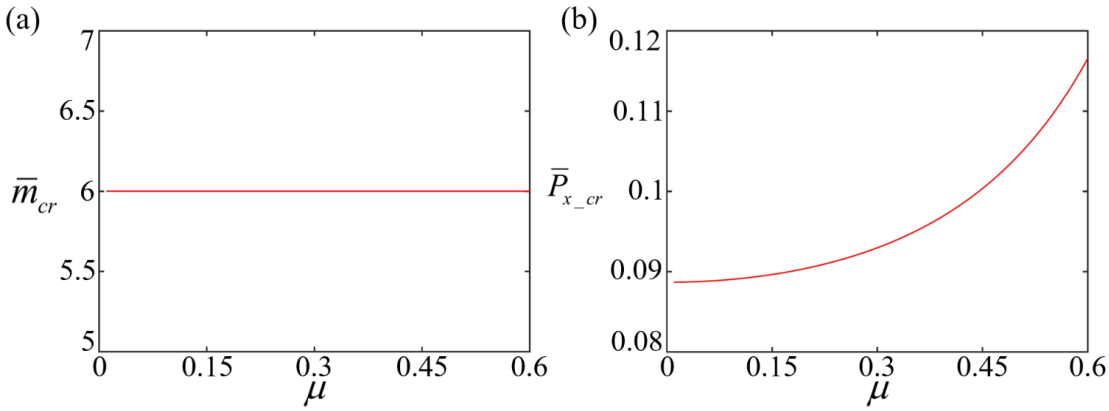


Figure 13. Effect of the Poisson's ratio μ on dimensionless critical buckling load $\overline{P}_{x_cr}$ and dimensionless critical buckling wave number $\overline{m}_{cr}$ for $\overline{b} = 0.24$, $\overline{E}_2 = 1$, $\overline{t}_1 = 0.015$, $\overline{t}_2 = 0.012$, $\lambda = 1$ and $\overline{\xi} = 0.5$. (**a**): Dependence of the dimensionless critical buckling wave number $\overline{m}_{cr}$ on the Poisson's ratio μ; (**b**): Dependence of the dimensionless critical buckling load $\overline{P}_{x_cr}$ on the Poisson's ratio μ.

4.7. Effect of the Rotational Restraint Stiffness

In the calculation, we give the dimensionless parameters $\overline{b} = 0.24$, $\overline{E}_2 = 1$, $\overline{t}_1 = 0.015$, $\overline{t}_2 = 0.012$, $\lambda = 1$ and $\mu = 0.3$. As shown in Figure 14, within the given range of dimensionless parameters, the dimensionless critical buckling wave number $\overline{m}_{cr}$ remains constant as the dimensionless rotational restraint stiffness $\overline{\xi}$ increases. However, the dimensionless critical buckling load $\overline{P}_{x_cr}$ gradually increases with the increase in rotational restraint stiffness. This result occurs because variations in rotational restraint stiffness within this range do not affect the wavelength of the composite structure; thus, the wave number remains unchanged. As the rotational restraint stiffness increases, the resistance to rotation of the composite CSP pipe-arch is enhanced, thereby improving the overall strength of the composite structure. Consequently, a higher load is required to bring the composite CSP pipe-arch structure to its critical buckling point, resulting in a gradual increase in the critical buckling load.

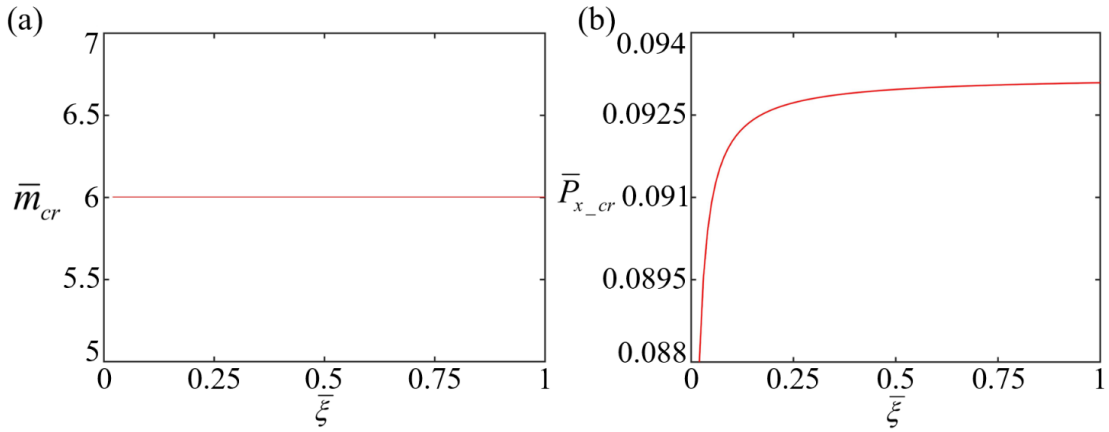


Figure 14. Effect of the rotational restraint stiffness $\overline{\xi}$ on dimensionless critical buckling load $\overline{P}_{x_cr}$ and dimensionless critical buckling wave number $\overline{m}_{cr}$ for $\overline{b} = 0.24$, $\overline{E}_2 = 1$, $\overline{t}_1 = 0.015$, $\overline{t}_2 = 0.012$, $\lambda = 1$ and $\mu = 0.3$. (**a**) Dependence of the dimensionless critical buckling wave number $\overline{m}_{cr}$ on the dimensionless rotational restraint stiffness $\overline{\xi}$. (**b**) Dependence of the dimensionless critical buckling load $\overline{P}_{x_cr}$ on the dimensionless rotational restraint stiffness $\overline{\xi}$.

The individual parameter buckling analysis results in this section align with the physical intuition. For instance, increasing the aspect ratio b/a of the straight part of the CSP pipe-arch reduces structural stability, which is consistent with existing research. Additionally, increasing the thickness $\overline{t}_1$, $\overline{t}_2$, the elastic modulus ratio E_2/E_1, the interlayer bonding coefficient λ, the Poisson's ratio μ, and the rotational restraint stiffness $\overline{\xi}$ all enhance local stability. These findings indirectly reflect the reliability of the proposed expression, further validated by the results in Section 3.

4.8. Coupling Effects Between Key Parameters

In the calculations for Figure 15a, we set the dimensionless parameters $\overline{E}_2 = 1$, $\overline{t}_2 = 0.012$, $\lambda = 1$, $\mu = 0.3$ and $\overline{\xi} = 0.5$. For Figure 15b, the dimensionless parameters $\overline{E}_2 = 1$, $\overline{t}_2 = 0.012$, $\lambda = 1$, $\mu = 0.3$ and $\overline{b} = 0.24$ are given. For Figure 15c, the parameters $\overline{E}_2 = 1$, $\overline{t}_2 = 0.012$, $\lambda = 1$, $\mu = 0.3$ and $\overline{t}_1 = 0.015$. are set.

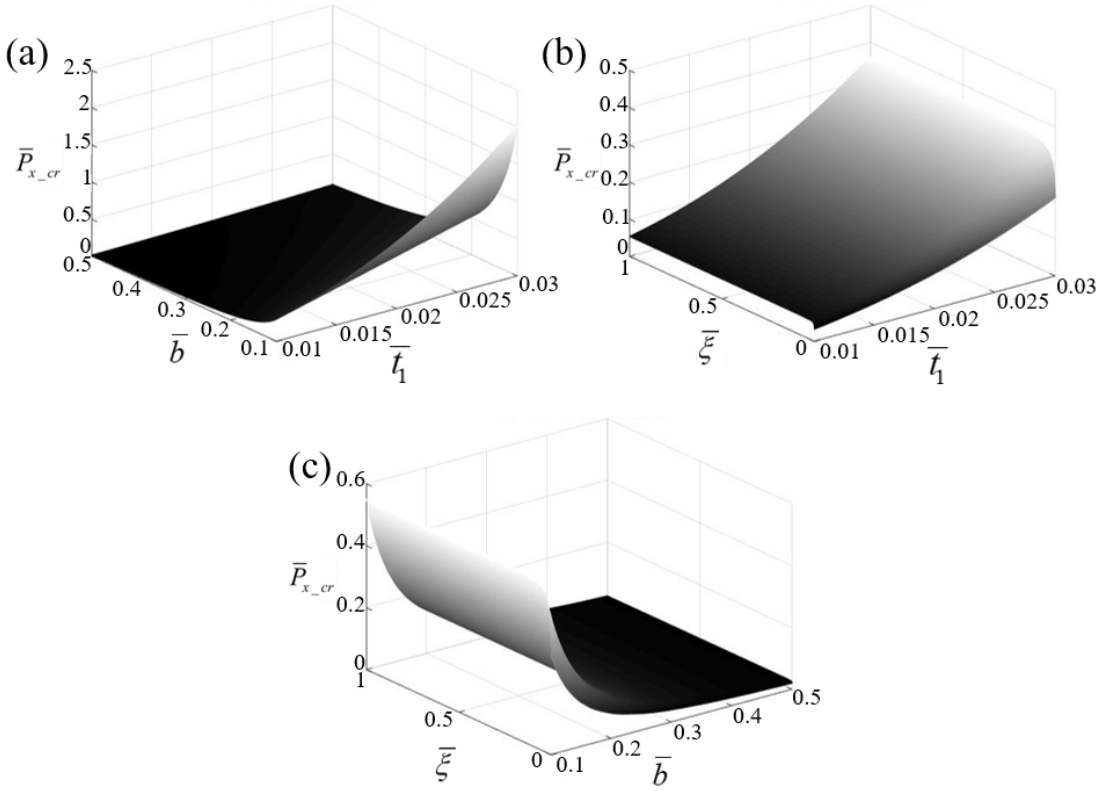


Figure 15. The effect of coupling among parameters $\overline{t}_1$, $\overline{b}$, and $\overline{\xi}$ related to the transverse direction bending stiffness of the plate on the critical buckling load $\overline{P}_{x_cr}$. (**a**) The effect of coupling between the dimensionless width of the straight part $\overline{b}$ and the thickness of the corrugated steel layer $\overline{t}_1$ on the critical buckling load. (**b**) The effect of coupling between the dimensionless rotational restraint stiffness $\overline{\xi}$ and the thickness of the corrugated steel layer $\overline{t}_1$ on the critical buckling load. (**c**) The effect of coupling between the dimensionless rotational restraint stiffness $\overline{\xi}$ and the width of the straight part $\overline{b}$ on the critical buckling load.

From Figure 15a, it can be seen that increasing $\overline{t}_1$ while decreasing $\overline{b}$ maximizes the critical buckling load. This parameter coupling significantly enhances the bending stiffness of the plate, thereby improving its resistance to instability. Simply increasing $\overline{t}_1$ or decreasing $\overline{b}$ alone is less effective than increasing $\overline{t}_1$ while simultaneously decreasing $\overline{b}$. Figure 15b shows that although increasing $\overline{\xi}$ can somewhat enhance the critical buckling load, the effect is far less significant than the increase in $\overline{t}_1$, indicating that the contribution of $\overline{\xi}$ to the plate's bending stiffness is less than that of $\overline{t}_1$. Figure 15c similarly shows that the contribution of $\overline{\xi}$ to the plate's bending stiffness is less than the effect of decreasing $\overline{b}$.

In summary, considering that $\overline{t}_1$, $\overline{b}$, and $\overline{\xi}$ parameters are related to the plate's transverse bending stiffness, analyzing the coupling effects of these parameters on the critical buckling load reveals that structural instability is influenced not only by individual parameters but also by their coupling effects. In practical applications, the coupling effects of parameters should be comprehensively considered to provide more effective guidance for design.

5. Conclusions

This paper analyzes the local buckling stability problem of the straight part of a composite CSP pipe-arch in soil. Based on elastic stability theory, a theoretical mechanical model of composite CSP pipe-arch is proposed. Rayleigh–Ritz and semi-combined composite structure stiffness approximate calculation methods are used to derive the theoretical formula for the elastic local buckling of the linear part of the composite structure.

Through theoretical analysis and numerical solution, the local buckling stability problem of composite CSP pipe-arch is theoretically analyzed.

(1) The bearing capacity of composite CSP pipe-arch includes a critical buckling load and a corresponding critical buckling wave number. When the local bearing capacity reaches this critical buckling load, the composite structure will undergo local instability.
(2) Through the analysis of individual parameters and the effects of parameter coupling, it is found that the local critical bearing capacity of the composite structure changes differently with the changes in parameters such as the side length of the straight part, the elastic modulus of the material, and the thickness.
(3) This paper proposes considering the bonding degree of composite CSP pipe-arch by using the inter-layer bonding coefficient, which in turn affects the stability of the composite structure. It is found that as the inter-layer bonding coefficient increases, the local stability of the composite structure is improved. The introduction of the interlayer bonding coefficient can more accurately analyze the local stability of the composite CSP pipe-arch.
(4) The method for analyzing the local buckling stability of composite CSP pipe-arch proposed in this paper takes into account the unique corrugated shape of the steel, the material properties of the composite layers, and the degree of bonding within the composite structure. This approach allows for a more accurate assessment of the local stability of composite CSP pipe-arch under compressive states. Through local buckling stability analysis, the stability of the structure can be precisely predicted during the design phase, effectively mitigating potential safety risks. This not only enhances the design quality of composite CSP pipe-arch, ensuring the safety, reliability, and economic efficiency of engineering projects but also aids in optimizing material usage, thereby maximizing cost-effectiveness.

Although pure critical buckling analysis provides a key indicator of instability, extending it to the actual load-bearing capacity of a structure requires considering material and geometric nonlinear effects. Future research could further explore these effects through nonlinear finite element analysis or validate the accuracy of models through experiments, thereby making the analysis results closer to real-world conditions. Additionally, in this study, the ξ and λ parameters are theoretical parameters derived from pure theoretical analysis to deduce the buckling load of composite CSP pipe-arch. These parameters help us construct theoretical models and understand the buckling characteristics of the structure within a purely theoretical framework. However, their actual values are currently difficult to determine, and in practical applications, further experiments or numerical simulations may be needed to more accurately determine their value ranges. Finally, simplifications in our study may impact the applicability of our findings to real-world scenarios. Therefore, it is essential to conduct future experimental validations to refine and confirm our results, thereby bridging the gap between theoretical analysis and practical application.

Author Contributions: Conceptualization, K.L.; methodology, C.C.; software, P.H.; validation, F.S.; investigation, C.C. and P.H.; data curation, F.S., P.X. and J.L.; writing—original draft, C.C.; writing—review and editing, K.L. and P.H.; supervision, K.L. All authors have read and agreed to the published version of the manuscript.

Funding: This study is supported by University Natural Science Research Project of Anhui Province (Nos. 2022AH030035 and 2022AH020029), National Natural Science Foundation of China (Grant No. 12172001), Anhui Provincial Natural Science Foundation (No. 2208085Y01), Outstanding Talents Cultivation Project of Universities in An-hui (No. gxyg2022029) and Research Project of China First Highway Engineering Co., Ltd. (T-GL-ZCBGS(J)-ANH-HZ-02-JS-032).

Data Availability Statement: Data are contained within the article.

Conflicts of Interest: Authors Chengwen Che and Pingping Hu were employed by the company China First Highway Engineering Co., Ltd. The remaining authors declare that the research was conducted in the absence of any commercial or financial relationships that could be construed as a

potential conflict of interest. The authors declare that this study received funding from China First Highway Engineering Co., Ltd. The funder was not involved in the study design, collection, analysis, interpretation of data, the writing of this article or the decision to submit it for publication.

References

1. Sha, A.; Jiang, W.; Shan, J.; Wu, W.; Li, Y.; Zhang, S. Pavement Structure and Materials Design for Sea-Crossing Bridges and Tunnels: Case Study of the Hong Kong–Zhuhai–Macau Bridge. *J. Road Eng.* **2022**, *2*, 99–113. [CrossRef]
2. Fragkakis, N.; Marinelli, M.; Lambropoulos, S. Preliminary Cost Estimate Model for Culverts. *Procedia Eng.* **2015**, *123*, 153–161. [CrossRef]
3. Germaniuk, K.; Gajda, T.; Sakowski, A.; Wierzbicki, T.; Kamiński, P. Bridge Structures Cracks: What Made That Phenomenon So Common? *Transp. Res. Procedia* **2016**, *14*, 4030–4039. [CrossRef]
4. Kuliczkowska, E. An Analysis of Road Pavement Collapses and Traffic Safety Hazards Resulting from Leaky Sewers. *Balt. J. Road Bridge Eng.* **2016**, *11*, 251–258. [CrossRef]
5. Rejab, M.R.M.; Ushijima, K.; Cantwell, W.J. The Shear Response of Lightweight Corrugated Core Structures. *J. Compos. Mater.* **2014**, *48*, 3785–3798. [CrossRef]
6. Nie, J.G.; Zhu, L.; Tao, M.X.; Tang, L. Shear Strength of Trapezoidal Corrugated Steel Webs. *J. Constr. Steel Res.* **2013**, *85*, 105–115. [CrossRef]
7. Yeau, K.Y.; Sezen, H.; Fox, P.J. Load Performance of In Situ Corrugated Steel Highway Culverts. *J. Perform. Constr. Facil.* **2009**, *23*, 32–39. [CrossRef]
8. Kananen, M.; Mäntyjärvi, K.; Keskitalo, M.; Hietala, M.; Järvenpää, A.; Holappa, K.; Saine, K.; Teiskonen, J. Laser Welded Corrugated Steel Panels in Industrial Applications. *Phys. Procedia* **2015**, *78*, 202–209. [CrossRef]
9. Sargand, S.M.; Khoury, I.; Hussein, H.H.; Masada, T. Load Capacity of Corrugated Steel Pipe with Extreme Corrosion under Shallow Cover. *J. Perform. Constr. Facil.* **2018**, *32*, 04018050. [CrossRef]
10. Ezzeldin, I.; El Naggar, H.; Newhook, J.; Jarjoura, G. Accelerated Wet/Dry Corrosion Test for Buried Corrugated Mild Steel. *Case Stud. Constr. Mater.* **2022**, *17*, e01152. [CrossRef]
11. Zhang, B.; Chen, W.; Xu, J. Mechanical Behavior of Prefabricated Composite Box Girders with Corrugated Steel Webs Under Static Loads. *J. Bridge Eng.* **2018**, *23*, 04018077. [CrossRef]
12. Zhang, H.; Liu, S.; Sun, L.; Zhao, Y. Study on Mechanical Properties of Corrugated Steel Support Tunnel Under Fault Sliding. *Eng. Comput.* **2023**, *40*, 3116–3135. [CrossRef]
13. Zhou, M.; Liu, Z.; Zhang, J.; An, L. Deformation Analysis of a Non-Prismatic Beam with Corrugated Steel Webs in the Elastic Stage. *Thin-Walled Struct.* **2016**, *109*, 260–270. [CrossRef]
14. Bian, X.; Tang, X.; Shen, W.; Ling, D.; Chen, Y. An Experimental Study on a Culvert Buried in Granular Soil Subjected to Vehicle Loads. *Adv. Struct. Eng.* **2012**, *15*, 1031–1040. [CrossRef]
15. Chen, T.; Su, M.; Pan, C.; Zhang, L.; Wang, H. Local Buckling of Corrugated Steel Plates in Buried Structures. *Thin-Walled Struct.* **2019**, *144*, 106348. [CrossRef]
16. Du, G.; Pettersson, L.; Karoumi, R. Soil-Steel Composite Bridge: An Alternative Design Solution for Short Spans Considering LCA. *J. Clean. Prod.* **2018**, *189*, 647–661. [CrossRef]
17. He, J.; Wang, S.; Liu, Y.; Dai, L.; Lyu, Z.; Li, C.; Xin, H.; Tan, C. The Development of Composite Bridges with Corrugated Steel Webs in China. *Proc. Inst. Civ. Eng. Bridge Eng.* **2021**, *174*, 28–44. [CrossRef]
18. Emami, F.; Mofid, M.; Vafai, A. Experimental Study on Cyclic Behavior of Trapezoidally Corrugated Steel Shear Walls. *Eng. Struct.* **2013**, *48*, 750–762. [CrossRef]
19. Hosseinzadeh, L.; Emami, F.; Mofid, M. Experimental Investigation on the Behavior of Corrugated Steel Shear Walls Subjected to Different Angles of Trapezoidal Plates. *Struct. Des. Tall Spec. Build.* **2017**, *26*, e1390. [CrossRef]
20. Jiang, R.J.; Au, F.T.K.; Xiao, Y.F. Prestressed Concrete Girder Bridges with Corrugated Steel Webs. *J. Struct. Eng.* **2015**, *141*, 04014108. [CrossRef]
21. Pradena, M.; Houben, L. Load Transfer-Crack Width Relation of Non-Dowelled Jointed Plain Concrete Short Slabs. *Balt. J. Road Bridge Eng.* **2018**, *13*, 40–45. [CrossRef]
22. Zhou, M.; Li, Y.; Han, Y.; Ni, P.; Qin, X.; Zhang, Y. Structural Response of Corrugated Steel Utility Tunnel During Backfilling Process and Under Surface Surcharge Pressures. *Acta Geotech.* **2023**, *18*, 1479–1494. [CrossRef]
23. Gajdzicki, M.; Perliński, W.; Michalak, B. Stability Analysis of Bi-Directionally Corrugated Steel Plates with Orthotropic Plate Model. *Eng. Struct.* **2018**, *160*, 519–534. [CrossRef]
24. Iwicki, P.; Rejowski, K.; Tejchman, J. Stability of Cylindrical Steel Silos Composed of Corrugated Sheets and Columns: FE Analyses Versus Eurocode 3 Approach. *Eng. Fail. Anal.* **2015**, *57*, 444–469. [CrossRef]
25. Jiang, Z.; Niu, Z.; Zhang, A.; Liu, X. Design Method of Axial Compression Stability for Cross-Section Corrugated Plate Steel Special-Shaped Columns. *Thin-Walled Struct.* **2024**, *194*, 111243. [CrossRef]
26. Wu, L.L.; An, L.P.; Bai, Y. In-Plane Stability of Steel Circular Closed Supports with I-Section of Sinusoidal Corrugated Webs: Experimental and Numerical Study. *Tunn. Undergr. Space Technol.* **2020**, *106*, 103566. [CrossRef]
27. Elkawas, A.A.; Hassanein, M.F.; Elchalakani, M. Lateral-Torsional Buckling Strength and Behavior of High-Strength Steel Corrugated Web Girders for Bridge Construction. *Thin-Walled Struct.* **2018**, *122*, 112–123. [CrossRef]

28. Li, G.Q.; Jiang, J.; Zhu, Q. Local Buckling of Compression Flanges of H-Beams with Corrugated Webs. *J. Constr. Steel Res.* **2015**, *112*, 69–79. [CrossRef]
29. Sun, H.J.; Guo, Y.L.; Wen, C.B.; Zuo, J.Q. Local and Global Buckling Prevention Design of Corrugated Steel Plate Shear Walls. *J. Build. Eng.* **2023**, *68*, 106055. [CrossRef]
30. Wang, T.; Ma, J.; Wang, Y. Normalized Shear Strength of Trapezoidal Corrugated Steel Webs Dominated by Local Buckling. *Eng. Struct.* **2021**, *233*, 111909. [CrossRef]
31. Machimdamrong, C.; Watanabe, E.; Utsunomiya, T. Shear Buckling of Corrugated Plates with Edges Elastically Restrained Against Rotation. *Int. J. Struct. Stab. Dyn.* **2004**, *4*, 89–104. [CrossRef]
32. Dou, C.; Jiang, Z.Q.; Pi, Y.L.; Guo, Y.L. Elastic Shear Buckling of Sinusoidally Corrugated Steel Plate Shear Walls. *Eng. Struct.* **2016**, *121*, 136–146. [CrossRef]
33. Dou, C.; Pi, Y.L.; Gao, W. Shear Resistance and Post-Buckling Behavior of Corrugated Panels in Steel Plate Shear Walls. *Thin-Walled Struct.* **2018**, *131*, 816–826. [CrossRef]
34. Li, B.J.; Zhu, L.S.; Fu, X.S. Theoretical Analysis for Local Buckling of Corrugated Steel Plate. *E3S Web Conf.* **2018**, *38*, 03002. [CrossRef]
35. Bi, C.; Wang, Y.B.; Liu, X.Y.; Jiao, Z.L. Buckling Analysis and Experimental Study of Simply-Supported Single-Corrugation Steel Plates Subjected to Compression. *Thin-Walled Struct.* **2022**, *172*, 108850. [CrossRef]
36. Guo, T.; Sause, R. Analysis of Local Elastic Shear Buckling of Trapezoidal Corrugated Steel Webs. *J. Constr. Steel Res.* **2014**, *102*, 59–71. [CrossRef]
37. Liu, T.; Song, B.; Huang, G.; Jiang, X.; Guo, S.; Zheng, K.; Pan, F. Preparation, Structure and Properties of Mg/Al Laminated Metal Composites Fabricated by Roll-Bonding, a Review. *J. Magnes. Alloy.* **2022**, *10*, 2062–2093. [CrossRef]
38. Cheng, Z.; Zhang, Q.; Bao, Y.; Deng, P.; Wei, C.; Li, M. Flexural Behavior of Corrugated Steel-UHPC Composite Bridge Decks. *Eng. Struct.* **2021**, *246*, 113066. [CrossRef]
39. Guo, C.; Wang, Z.; Zhao, H.; Zhou, Z.; Wang, M. Numerical Simulation of Corrugated Steel Concrete Prefabricated Support Structure for Underground Engineering. *Sustainability* **2023**, *15*, 14495. [CrossRef]
40. Guo, S.; He, X.; He, H.; Li, Z.; Zeng, Y.; Tan, H.; Zhou, J. Study on Shear Resistance and Structural Performance of Corrugated Steel–Concrete Composite Deck. *Appl. Sci.* **2023**, *13*, 10112. [CrossRef]
41. Guo, Y.L.; Wen, C.B.; Sun, H.J. Study and Application of Steel and Composite Walls with Corrugated Steel Plates in China. *Int. J. Struct. Stab. Dyn.* **2023**, *23*, 2340024. [CrossRef]
42. Bui, V.T.; Truong, V.H.; Trinh, M.C.; Kim, S.E. Fully Nonlinear Analysis of Steel-Concrete Composite Girders with Web Local Buckling Effects. *Int. J. Mech. Sci.* **2020**, *184*, 105729. [CrossRef]
43. John, K.; Ashraf, M.; Weiss, M.; Al-Ameri, R. E Experimental Investigation of Novel Corrugated Steel Deck under Construction Load for Composite Slim-Flooring. *Buildings* **2020**, *10*, 208. [CrossRef]
44. Wang, M.Z.; Guo, Y.L.; Zhu, J.S.; Yang, X. Flexural-Torsional Buckling and Design Recommendations of Axially Loaded Concrete-Infilled Double Steel Corrugated-Plate Walls with T-Section. *Eng. Struct.* **2020**, *208*, 110345. [CrossRef]
45. Zamanifar, H.; Sarrami-Foroushani, S.; Azhari, M. A Parametric Study on the Mechanical and Thermal Stability of Corrugated-Core Sandwich Plates. *Structures* **2020**, *24*, 209–226. [CrossRef]
46. El-Taher, M. The Effect of Wall and Backfill Soil Deterioration on Corrugated Metal Culvert Stability. Ph.D. Thesis, Queen's University, Kingston, ON, Canada, 2009.
47. Wang, M.Z.; Guo, Y.L.; Yang, X.; Zhu, J.S. Compressive Buckling Behavior of Steel Corrugated Plates in Contact with a Rigid Medium. *Compos. Struct.* **2021**, *262*, 113356. [CrossRef]
48. Kheirikhah, M.M.; Babaghasabha, V. Bending and Buckling Analysis of Corrugated Composite Sandwich Plates. *J Braz. Soc. Mech. Sci. Eng.* **2016**, *38*, 2571–2588. [CrossRef]
49. Guo, Y.L.; Zhu, J.S.; Wang, M.Z.; Yang, X.; Zhou, P. Overall Instability Performance of Concrete-Infilled Double Steel Corrugated-Plate Walls. *Thin-Walled Struct.* **2018**, *130*, 372–394. [CrossRef]
50. Liu, B.; Zhang, Z.; Zhang, M.; Wang, X. Experimental Study of the Mechanical Performance of Corrugated Steel Plate-Concrete Composite Structures. *Int. J. Steel Struct.* **2019**, *19*, 733–746. [CrossRef]
51. Zhang, J.L.; Liu, B.D.; Liu, R. Behavior of Sinusoidal-Corrugated-Steel-Plate–Concrete Composite Slabs: Experimental Investigation and Theoretical Model Development. *J. Constr. Steel Res.* **2021**, *187*, 106958. [CrossRef]
52. Sun, D.; Liu, C.; Wang, Y.; Xia, Q.; Liu, F. Static Performance of a New Type of Corrugated Steel-Concrete Composite Shell Under Mid-Span Loading. *Structures* **2022**, *37*, 109–124. [CrossRef]
53. Rauch, A.F.; Sargand, S.M.; Hazen, G.A. Behavior of Deeply Corrugated Steel Plate in Culvert. *J. Struct. Eng.* **1994**, *120*, 1651–1655. [CrossRef]
54. Naghdi, P.M.; Trapp, J.A. On the General Theory of Stability for Elastic Bodies. *Arch. Ration. Mech. Anal.* **1973**, *51*, 165–191. [CrossRef]
55. Naghdi, P.M.; Trapp, J.A. Experimental and Theoretical Correlations for Elastic Buckling of Axially Compressed Ring-Stiffened Cylinders. *J. Strain Anal. Eng. Des.* **1983**, *18*, 81–93. [CrossRef]
56. Cai, J.; Long, Y.L. Local Buckling of Steel Plates in Rectangular CFT Columns with Binding Bars. *J. Constr. Steel Res.* **2009**, *65*, 965–972. [CrossRef]

57. Long, Y.L.; Wan, J.; Cai, J. Theoretical Study on Local Buckling of Rectangular CFT Columns Under Eccentric Compression. *J. Constr. Steel Res.* **2016**, *120*, 70–80. [CrossRef]
58. Zhi, T. Simplified Calculation of Bi-Layer Plate Bending with Semi-Continuous Condition. *Highway* **2001**, *4*, 25–26.

Disclaimer/Publisher's Note: The statements, opinions and data contained in all publications are solely those of the individual author(s) and contributor(s) and not of MDPI and/or the editor(s). MDPI and/or the editor(s) disclaim responsibility for any injury to people or property resulting from any ideas, methods, instructions or products referred to in the content.